ELSEVIER

Contents lists available at ScienceDirect

Surface & Coatings Technology

journal homepage: www.elsevier.com/locate/surfcoat



Characterization of a versatile low-pressure plasma treatment unit for steel surfaces

Gustav Gürtler a,b,*, Wolfgang Burgstaller , Friedrich Aumayr b, Markus Valtiner b

ARTICLE INFO

Keywords: Low-pressure plasma Steel Surface activation Optical emission spectroscopy Retarding field energy analyzer

ABSTRACT

This study presents a thorough characterization of a low-pressure plasma treatment applied to low-carbon steel surfaces conducted in a simple and versatile plasma treatment unit. Optical emission spectroscopy (OES) and retarding field energy analyzer (RFEA) measurements are utilized to investigate plasma parameters and sample surface interactions. OES confirms sputtering of the sample surface, while the energy and ion flux can be independently tuned by varying the voltage of the plasma generator and adjusting the supportive plasma discharge sustained by a thermionic electron emitter. The study measures electron temperatures ranging from T_e = 1~eV~to~2~eV and ion flux densities up to $J_i = 7~A/m^2$. Mapping of the ion flux density on the sample surface reveals a distribution consistent with the geometry of the anode tube implemented. Plasma treated steel surfaces are investigated via contact angle measurements and X-ray photoelectron spectroscopy. Results indicate an increase in surface free energy following short plasma treatment at an energy density of approximately $E_A \approx 5~J/cm^2$. This can improve adhesion in coatings or bonding processes, making low-pressure plasma treatment highly suitable for various industrial applications. Additionally, the effective reduction of carbon compounds and oxides on steel surfaces suggests potential uses in manufacturing sectors that require clean, reactive metal surfaces for improved performance and longevity.

1. Introduction

Low-pressure plasmas find wide application in several sectors of research and industry due to their high chemical reactivity at comparably low temperatures, non-destructive nature, environmental friend-liness, and good controllability even though they require vacuum equipment which is often costly [1–3]. They are utilized for deposition of thin films in the microelectronic industry, machinery, and optics [3,4], as well as adhesion improvements of polymeric surfaces [5,6], plasma modifications of textiles [7], plasma sterilization for medical applications [8–10], and plasma dry-etching in semiconductor industry [11–13]. Applications of low-pressure plasma treatments of steel surfaces are mainly focused on plasma-assisted thermochemical treatments for surface hardening of stainless steels [14,15], plasma activation [16,17], plasma cleaning [18–20], and plasma (–enhanced) coating [21–25].

In this paper, a simple and versatile low-pressure plasma treatment unit designed for batch low-carbon steel samples is introduced, which is intended as pre-treatment step before subsequent processing. A characterization of the pulsed-DC plasma is necessary to control and optimize the applied plasma treatment. Optical emission spectroscopy (OES), which is a powerful tool to perform in-situ diagnostics of lowpressure plasmas without influencing the plasma parameters by invasive probes is employed for monitoring the plasma treatment. It is a simple and inexpensive tool to determine physical and chemical parameters and identify different atomic species or molecules by their characteristic emission spectra [26]. As an additional plasma diagnostic tool, a retarding field energy analyzer (RFEA) is implemented, which is an electrical probe commonly used in plasma characterization [27]. RFEAs are employed for the determination of ion energy distributions (IEDs) since several decades due to their simple use and easy application [28,29]. RFEA probes can be placed on grounded or, if appropriately electrically filtered, biased surfaces as well [30]. Typically, the sensor consists of one or several orifices enabling the charged particles to enter, being backed by several fine meshes, which discriminate the charged particles by applying a retarding voltage due to their energy before reaching a collector plate [31]. Its strength lies in its ability to accurately determine the flux and energy of ions impinging on surfaces exposed to

a voestalpine Stahl GmbH, voestalpine Straße 3, 4020, Linz, Austria

b Institute of Applied Physics, TU Wien, Wiedner Hauptstraße 8-10/E134, 1040, Wien, Austria

^{*} Corresponding author at: voestalpine Stahl GmbH, voestalpine Straße 3, 4020, Linz, Austria. *E-mail address:* gustav.guertler@voestalpine.com (G. Gürtler).

the plasma. Surface modifications of plasma treated steel are assessed utilizing contact angle (CA) measurements, employing the sessile drop method, as well as X-ray photoelectron spectroscopy (XPS).

2. Experimental

The plasma treatment unit is built in cylindrical shape. The anode tube with an inner diameter of $d = 184.5 \, mm$ is electrically isolated and placed within the grounded cylindrical vacuum chamber, where base pressures of $p = 10^{-6}$ mbar can be achieved. In approximately d = 20 mm distance from the anode, a tungsten wire (length l = 450 mm, thickness t= 0.5 mm) is mounted as thermionic electron emitter, isolated from the anode. By applying a DC offset voltage U_{off} between the anode and the tungsten wire, a supportive discharge can be ignited, facilitating the ignition of the sample-treating plasma discharge via the plasma generator. Typically, the offset voltage is set to a constant value of $U_{off} = 50 \text{ V}$ that is always constant. The cylindrical design of the plasma treatment unit was selected to optimize the distribution and confinement of plasma. The anode tube is backed by a permanent magnetic array, confining the plasma to the anode tube. Both, the anode tube and the magnetic array are water cooled to prevent damage and demagnetization of the permanent magnets. A batch low-carbon steel sample, usually longer than the anode tube itself, is serving as cathode for the sampletreating plasma discharge. The sample piece is clamped at one end and inserted, with the other end first, into the anode tube using a push rod. A systematic setup of the plasma treatment unit during OES measurements is displayed in Fig. 1. The plasma generator utilized for the sample-treating discharge is an Advanced Energy Pinnacle Plus + power supply, providing a pulsed-DC or DC voltage U with tunable frequency and duty cycle.

Using argon as process gas, a working pressure in the range of $p=3 \times 10^{-3}$ mbar is set via a mass flow controller. Argon is utilized as a process gas due to its combination of low cost and inert nature avoiding chemical changes of the steel surface as well as the tungsten wire during plasma treatment. The parameters are adjusted in the range of generator voltages (U=50~V-400~V), frequencies (f=0~kHz-300~kHz) with duty cycles of 5 % to 45 % and a tungsten wire power $P_W=360~W-625~W$ resulting in a delivered average power density of approximately $P_A\approx 1~W~cm^{-2}$. Unless otherwise specified, all experiments in this work are

conducted at a standard parameter set, which is a pulsed-DC voltage U = 200 V, a working pressure $p = 3 \times 10^{-3}$, a frequency $f = 160 \, \text{kHz}$ with a pulse reverse time of $2.8 \, \mu s$, a DC offset voltage between the anode and the tungsten wire $U_{off} = 50 \text{ V}$ and a power to heat the tungsten wire P_W = 470 W to 480 W at a plasma treatment duration of t = 30 s. The ignited argon plasma is monitored by an Echelle type spectrometer (LLA Instrument GmbH, ESA4000plus) with a spectral resolution of $\lambda/\Delta\lambda$ = 19,500 and a spectral range of $\lambda = 200 \text{ nm} - 780 \text{ nm}$. The radiation emitted by the argon plasma and the tungsten wire is collected via an optical fiber and guided to the entrance slit of the spectrometer. For each OES spectrum investigated, 30 measurements are conducted, keeping all experimental parameters unchanged, resulting in an average spectrum with a typical relative standard deviation (RSD) < 5 %. Spectral intensity data are extracted from the OES spectra by self-written Python programs, integrating the area and determining the height of a Voigt profile fitted to the investigated emission peaks. Data processing is performed using commercially available software (Origin Pro, Origin-Lab Corporation). The identification of detected OES emission peaks is performed using NIST [32] and Kurucz [33] database.

In-situ plasma analysis is performed via a commercial retarding field energy analyzer (Semion Single/Multi System, Impedans Ldt.), which is set to cathode potential by being placed directly on the sample. A detailed description of the probe setup can be found elsewhere [28]. Briefly, the probe consists of a chassis, which is set to sample potential, orifices enabling the charged particles to enter the probe. The orifices are backed by four plane-parallel metal meshes with the aim of blocking unwanted charged particles, discriminating the entered particles according to their velocity, and screening secondary electrons being emitted from the collector plate, which is placed behind the metal meshes [34]. Time-averaged ion energy distributions (IEDs) are determined from averaged current- voltage characteristics by being smoothened and differentiated. The RFEA data are processed using software supplied by Impedans LDT.

Plasma treated steel surfaces are examined by contact angle (CA) measurements utilizing Krüss mobile surface analyzer which employs a liquid needle for static contact angle measurements [35]. Deionized water and diiodomethane are used as liquids for measuring the contact angle at eight different drop volumes (starting at $V=0.5~\mu l$, increasing in 0.2 $~\mu l$ steps), resulting in an average contact angle value. The

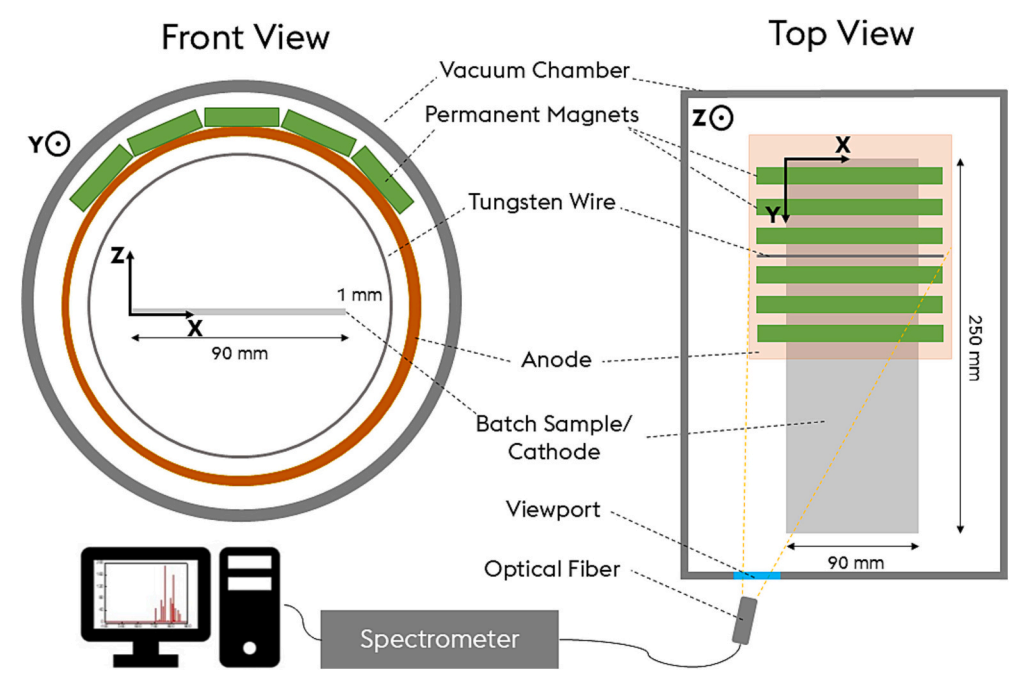


Fig. 1. Schematic setup of the investigated plasma treatment unit while performing OES measurements.

determination of the respective contact angles is performed by KRÜSS ADVANCE software. The calculation of total, dispersive, and polar free surface energies of plasma treated sample surfaces is done via the OWRK-model [36]. Alkaline cleaned steel substrate pieces $(15 \times 15 \times 1 \ mm^3)$ are positioned on top of a steel sample being plasma treated, after which they are investigated via CA measurements. This configuration produces both a plasma treated and an untreated substrate surface. The untreated surface serves as reference that was exposed to identical conditions regarding temperature, pressure, and gas environment as the plasma treated surface. The investigated sample is cooled to room temperature prior to contact angle measurements by pressurized air. The minimum time necessary for venting the vacuum system, cooling the sample and starting contact angle measurements is 120 s, which is of importance since contact angles are investigated as function of time the plasma treated surface is exposed to atmospheric conditions.

X-ray photoelectron spectroscopy (XPS) measurements are performed using a Versa Probe III spectrometer (Physical Electronics GmbH) equipped with a monochromatic Al K_{α} (1486.6 eV) source. The beam diameter is set 100 μm with a beam energy of 25 W. Spectra are detected from an area of 200 $\mu m \times 200~\mu m$, the electron takeoff angle is set to 45° relative to a normal surface. Survey scans are recorded applying pass energy of 140 eV and step width of 0.5 eV, while high resolution spectra are recorded at 27 eV and 0.05 eV steps. Steel substrates are mounted via polymeric tape, while a combination of electronic and ionic charge compensation is used. Data processing is performed utilizing CasaXPS (Version 2.3.26PR1.0). All peaks are fitted with Gaussian-Lorentzian peak shapes, while the binding energy of investigated species is in respect to C (1s) signal at 284.7 eV.

3. Results and discussion

3.1. Optical emission spectroscopy

OES spectra of the supportive discharge ignited between the heated tungsten wire and the anode reveal Ar (I) and Ar (II) emission lines. Notably absent are emission lines from elements on the sample surface, such as iron, indicating that sputtering of the sample does not occur without activating the pulsed-DC voltage. If the sample-treating plasma is ignited, multiple Fe (I) and Fe(II) emission lines are detected – including Fe (I) at $\lambda = 372.0$ nm and Fe (II) at $\lambda = 238.2$ nm- along with

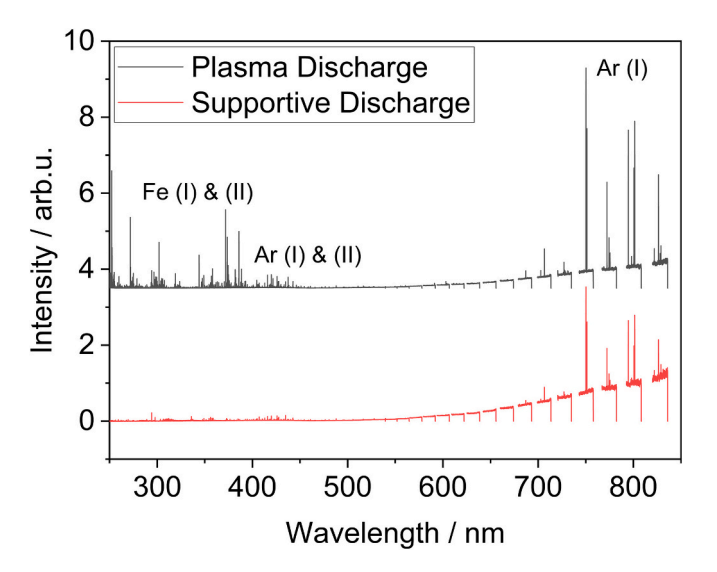


Fig. 2. Typical sensitivity-corrected OES spectra of the supportive discharge and the sample-treating plasma discharge, normalized to identical exposure times. The sample-treating plasma emits more intense argon emission lines compared to the supportive discharge as well as iron emission lines. For clarity, OES spectrum "Plasma discharge" is shown with offset.

trace elements such as Mn (I), exemplified by its emission line at $\lambda=403$ nm, as shown in Fig. 2. W (I) emission lines cannot be detected during plasma treatment. The presence of Fe (I) and (II) emission lines suggests that sputtering of the sample surface occurs due to the applied bias voltage. The detected argon emission lines are more intense by a factor x2-x3 ($\lambda<500$ nm) and up to x4-x5 ($\lambda>600$ nm) when the sample-treating plasma is activated.

Since the investigated optically thin plasma discharge is glowing at low pressure and typical power density of $P_A \approx 1~W~cm^{-2}$, the excitation of atoms and ions is assumed to be dominated by direct excitation from the ground state via electron impacts and de-excitation by radiative decay being described by the corona model [37]. F. J. Gordillo-Vázquez et al. [38] introduced a modified Boltzmann plot which enables the determination of the electron temperature T_e from neutral argon emission lines. The slope of the modified Boltzmann plot, described by Eq. (1)

$$ln\left(\frac{I_{ij}\lambda_{ij}\sum_{i>j}A_{ij}}{g_iA_{ij}b_{1j}}\right) = -\frac{E_{1i}}{k_BT_e} + C$$
(1)

is directly proportional to the electron temperature T_e (eV/k_B). Iii describes the emission intensity (arb.u.), λ_{ij} the wavelength of the emitted photon (nm), g_i the statistical weight of the upper level, A_{ii} the Einstein coefficient of the transition (s^{-1}), and E_i the upper state energy (eV). b_{1i} is a parameter determined from the energy E_{1i} and the electron collisional cross section from level 1 to j (m²), k_B describes the Boltzmann constant, and C is a constant [38-40]. The values for the parameter b_{1i} are taken from [38,41], while the optical absorption cross section values are reused from [42]. Table 1 summarizes the spectroscopic data of Ar (I) emission lines used in modified Boltzmann plots in this work, while Fig. 3 displays a typical modified Boltzmann plot. Utilizing the modified Boltzmann plot technique for various sets of parameters, the electron temperature T_e of the plasma discharge is determined to be in the range of $T_e = 1$ eV to 2 eV. Comparable electron temperatures have been reported in studies characterizing DC and pulsed-DC magnetron sputtering plasmas with argon as process gas [43,44]. Exemplarily, the electron temperature T_e as function of the working gas pressure (at otherwise constant standard parameters except the generator voltage of U = 300 V) is plotted in Fig. 4, showing a decreasing T_e with increasing working gas pressure caused by a reduction of the mean free path of free electrons due to higher collision frequency at higher pressures. This behavior is observed in several other technical low-pressure plasmas [45-47].

3.2. Retarding field energy analyzer

RFEA measurements reveal a pronounced, sharp rise in the detected current-voltage curve. This is characteristic for all experiments performed. This results in an ion energy distribution (IED) with a monoenergetic peak, and values close to zero elsewhere. This suggests that the ions sputtering the sample surface possess similar energy, which is expected for pulsed-DC low-pressure discharges [31,34], assuming a

Table 1Spectroscopic data of neutral Ar (I) emission lines used for modified Boltzmann plots.

Wavelength (nm)	A $_{ij}$ (10 ⁶ s ⁻¹)	$\sum\nolimits_{i>j} A_{ij} \; (10^6 \; {\rm s}^{-1})$	b_{1i}	E _i (eV)
516.22	1.90	2.86	6.83×10^{-11}	15.31
687.12	2.78	5.46	4.60×10^{-10}	14.72
703.00	2.67	5.72	3.23×10^{-10}	14.84
706.70	3.80	23.50	8.23×10^{-10}	13.30
720.68	2.48	5.44	2.59×10^{-10}	15.02
731.17	1.70	5.44	3.39×10^{-10}	14.85
750.39	45.00	45.20	2.73×10^{-9}	13.48
751.47	40.00	40.00	2.55×10^{-9}	13.28

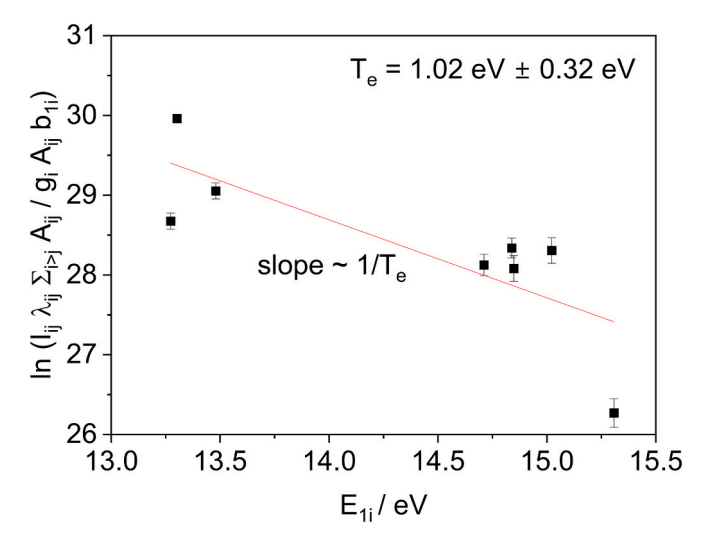


Fig. 3. Typical modified Boltzmann plot for determination of the electron temperature Te from several neutral Ar(I) emission lines.

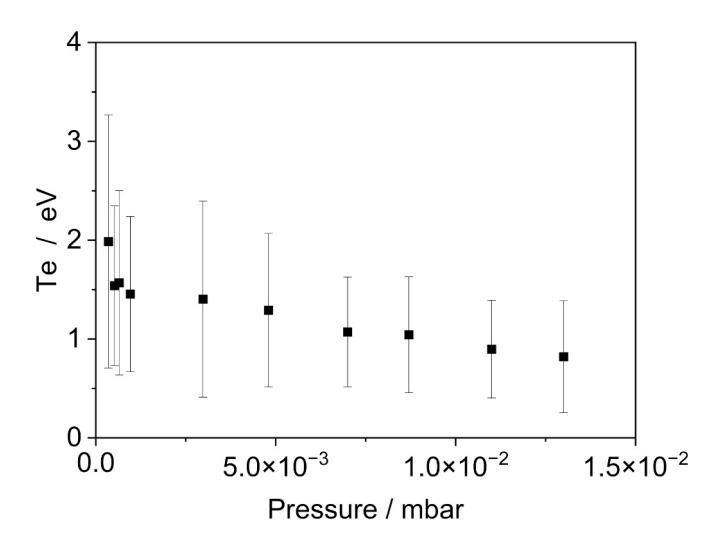


Fig. 4. Determined electron temperature T_e utilizing modified Boltzmann plots as a function of working gas pressure during plasma treatment of a steel sample.

collisionless plasma sheath and a charged-particles transition time through the sheath that is shorter than the period of the applied pulsed-DC voltage (in the standard case, $T=6.25\,\mu s$) [48]. Other shapes of IEDs, as the saddle-shaped IED described in similar pulsed-DC [34] and numerous RF discharges [28,49,50] could not be observed for the investigated parameter sets.

From the calculated IED, the total ion flux density J_i to the sample surface can be calculated using Eq. (2).

$$\int_{I}^{E_{max}} IED \, dE$$

$$J_{i} = \frac{E_{min}}{A \cdot T}$$
(2)

 J_i is the ion flux density (A/m^2) , E_{min} and E_{max} limit the investigated energy range (eV), $A=18.6\ mm^2$ is the area of the sensor orifices (m^2) , and T=0.0625 is the transmission factor of the probe's grids. J_i values are calculated using Semion software (typical RSD = 5 %). As an additional characteristic measurement parameter, the energy of the impinging ions, determined by the position of the distinct peak in the IED, is extracted from RFEA measurement data. A typical current-voltage behavior as well as its first derivative are plotted in Fig. 5,

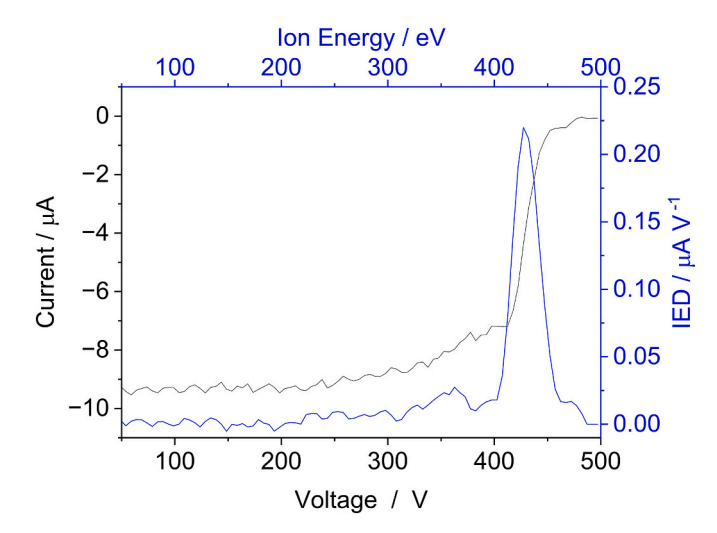


Fig. 5. Typical current-voltage characteristic detected with retarding field energy analyzer. From the first derivative of the I-U-characteristic, the ion energy distribution IED can be estimated.

which shows the results for a standard plasma parameter set, resulting in an ion flux density of $J_i = (2.6 \pm 0.1) \, \text{A/m}^2$. To gain information about the influence of respective setup parameters on the ion energy E and ion flux density J_i , individual parameters are sequentially varied while the others are kept constant at standard parameters. The results of varying the tungsten wire power P_W , controlling the electron current emitted from the thermionic electron emitter and therefore the charge carrier density of the supportive plasma discharge, and varying the generator

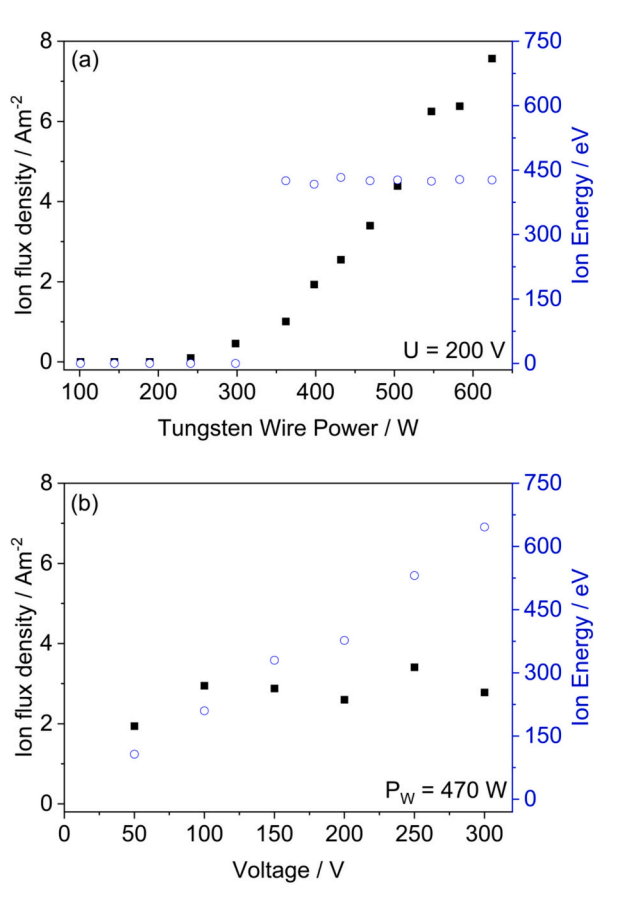
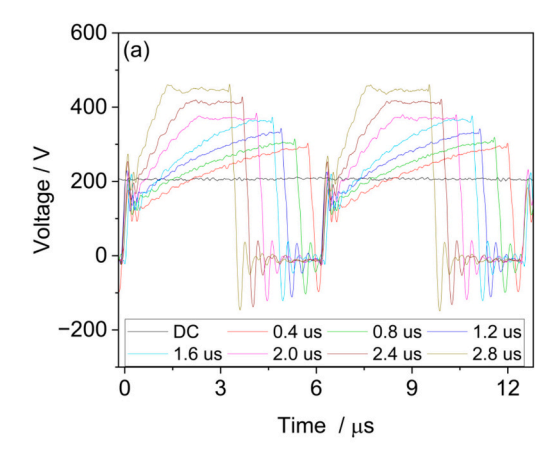


Fig. 6. Ion flux density and ion energy as function of (a) tungsten wire power P_W and (b) generator voltage U. While a change in P_W influences the ion flux density, the voltage shifts the energy of ions impinging the sample surface.

voltage U are shown in Fig. 6. The ion flux density J_i is greatly influenced by the tungsten wire power P_W , while the ion energy E and the FWHM of the IED peak is not affected (Fig. 6(a)). The increased temperature of the electron emitter, in accordance with Richardson's law, leads to an increased amount of thermionically emitted electrons, resulting in an increased ionization degree of the plasma and an enhanced ion flux J_i to the surface. Beneath a minimum electron current the surface-treating plasma is not ignited, leading to an ion flux close to $J_i = 0~A~m^{-2}$, highlighting the critical role of the supportive plasma discharge in enabling plasma treatment. A rise in applied generator voltage U results in an increased ion energy E impinging the substrate surface,

which is directly proportional, while the ion flux density J_i remains almost unchanged (Fig. 6(b)). Additionally, the FWHM of the detected peak of the IED is increasing from FWHM = 25 eV to 45 eV while increasing the generator voltage from U = 50 V to 300 V. The possibility of tuning the ion energy independently of the ion flux plotted density and vice versa is a major advantage of the described setup configuration allowing the tuneability of the plasma treatment to various subsequent working steps. The direct proportionality of the generator voltage U and the ion energy E is caused due to a change in sheath voltage, since the ion energy E is primarily determined by the plasma sheath compared to the time-averaged voltage displayed by the plasma generator and voltage accelerating the ions onto the surface. The reason for the observation of ions possessing approximately double the expected energy ($E = e \cdot |U|$) can be attributed to the waveform of the pulsed voltage signal, which applies significantly higher voltages as X-axis in Fig. 6. This is confirmed by oscilloscope measurements conducted during plasma treatments applying different duty cycles at identical frequency,



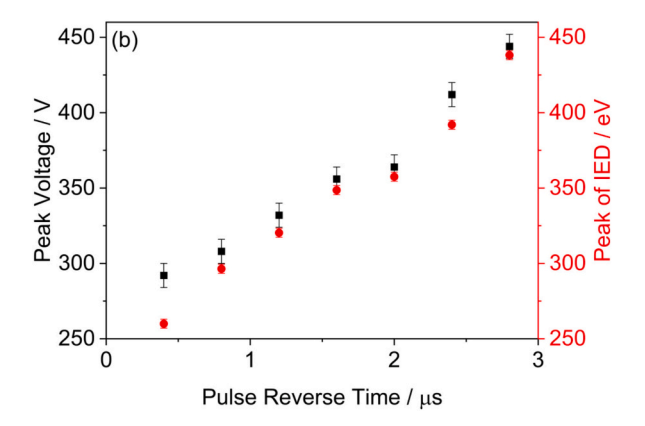


Fig. 7. (a) Voltage waveform generated by the pulsed-DC generator at various pulse reverse times for constant frequency $f=160\,$ kHz and time-averaged voltage of $U=200\,$ V. (b) Maximum voltage achieved during a single voltage pulse, and the peak of the IED determined via RFEA measurements as function of pulse reverse time for constant frequency and voltage.

as well as the respective determined energies of ions from the peak of the IEDF, depicted in Fig. 7.

Positioning the RFEA probe at different positions on the sample enables the determination of the spatial distribution of ions hitting the sample's topside surface during plasma treatments. Utilizing the IED obtained via the RFEA probe, a contour plot of the ion flux density (Fig. 8(a)) and the peak of the IED, corresponding to the ion energy E (Fig. 8(b)), can be created. No correlation can be recognized between the ion energy E impacting the sample surface and the location on the sample surface, most likely since it is influenced primarily by the plasma sheath voltage. The FWHM of detected IED peaks is close to constant at all sample positions, resulting in an average FWHM = 31.1 eV (STD: 5.0 eV). The ion flux density J_i increases in positions close to the tungsten wire (positioned at Y = 83 mm) and the corresponding supportive discharge. The pattern of the ion flux density map displayed in Fig. 8(a) can be explained by the geometry of the cylindrical anode tube and the non-radially symmetric sample. The elevated ion flux density on the left side of the sample (X < 45 mm) compared to the right side (X > 45 mm) is investigated and confirmed by welding two K-type thermocouples in the same distance from the center of the sample (X1 = 20 mm, X2 = 70mm) in the same Y-position Y = 80 mm. To exclude asymmetric influence of the tungsten wire, the sample is heated in a first experiment from room temperature up to 50 °C showing no asymmetry in the temperature distribution on the sample. Plasma treatment (same duration t = 30s as the heating via tungsten wire only) causes a greater temperature increase on the left (X1) thermocouple $\Delta T_{X1} = 116.1$ °C compared to the right (X2) thermocouple $\Delta T_{X2} = 81.6$ °C, supporting the findings of RFEA investigations. The reason for this asymmetric ion flux density is determined via Hall probe measurements, revealing a slight asymmetry in magnetic field lines promoting a higher ion flux density to the left side of the top of the sample, which results in an asymmetric plasma treatment.

3.3. Contact angle measurements

The influence of atmospheric conditions on the contact angle (CA) of plasma-treated surfaces is investigated since contact angle measurements are performed in atmosphere. For that purpose, CA measurements are conducted at various time intervals after the steel sample has been plasma treated at standard conditions and transferred from vacuum conditions to controlled atmospheric conditions. A strong increase in wettability t = 2 min after plasma treatment is observed for water compared to reference samples. With increasing time between plasma treatment and the time of atmospheric exposure, the water contact angle increases and then stabilizes near a constant value below that of the reference after an atmospheric exposure of approximately t = 4 h. In an additional experiment, a CA-reducing effect could still be observed t =80 h after plasma treatment. Utilizing the OWRK method, the dispersive and polar part of the surface free energy are determined and shown in Fig. 9. The total surface free energy as well as the polar surface free energy of plasma treated samples is strongly enhanced immediately after the treatment, while the disperse part is slightly reduced compared to reference measurements. With increasing exposure time to atmospheric conditions, the total and polar part of the surface energy is decreasing, saturating to a value greater than the reference, while the disperse part is slightly decreasing. This behavior is reflected in Fig. 9, where exponential decreasing fits are conducted for both the total and polar surface free energy, while the disperse part is described by a linear regression with a near-zero slope. The increase in surface energy results in enhanced adhesion properties of the steel surface, which is advantageous for applications such as coatings [18].

Due to strong influence of ambient conditions on the surface energy of plasma treated sample, it seems unlikely that changes in contact angles are due to variations in surface roughness. No influence of the plasma treatment on the surface roughness on a micron scale (lateral: $1.6~\mu m$, vertical $0.06~\mu m$) could be observed using white-light

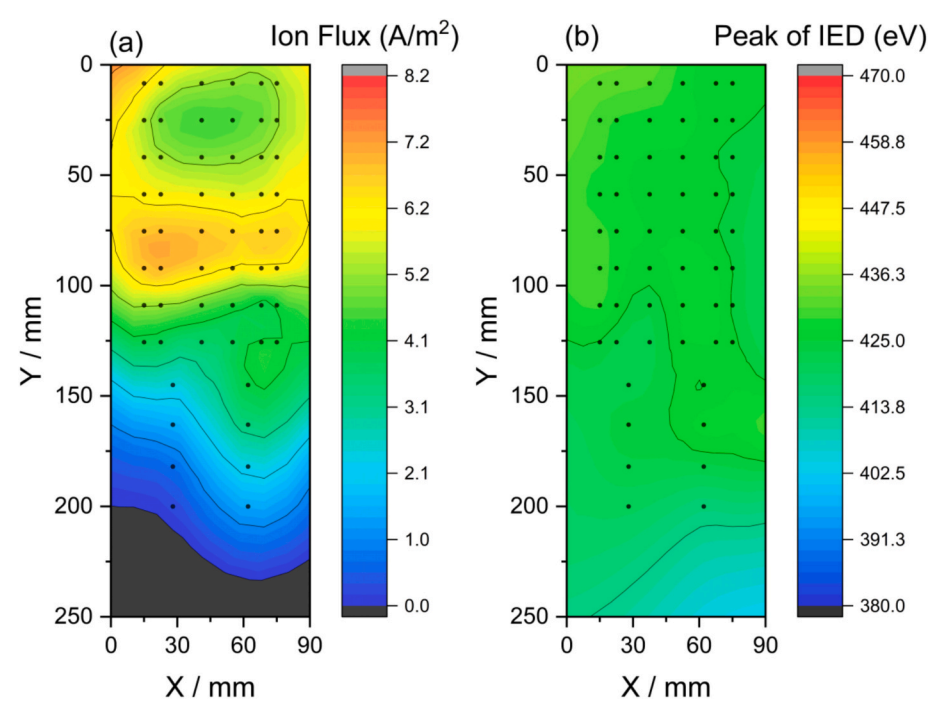


Fig. 8. Contour plots showing the spatial distribution of (a) ion flux impacting the sample surface and (b) the peak of the ion energy distribution (IED) detected via RFEA measurements.

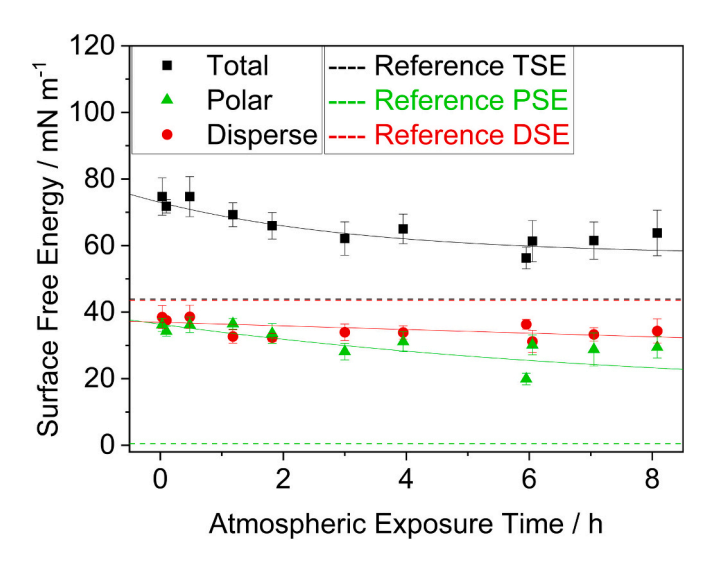


Fig. 9. The total, disperse, and free surface energy of the plasma treated steel surface are calculated from contact angle measurements using the OWRK method. The reference values, which are constant over time, are indicated with dashed lines in the respective colors.

interferometry ($S_a=0.98~\mu m$). To gain further insight into the influence of the plasma treatment on the surface roughness at smaller scales, atomic force microscope measurements are currently being conducted as part of our ongoing work.

To investigate the influence of plasma parameters on the steel substrate, generator voltages U, tungsten wire power P_W and plasma treatment time t are sequentially varied while other parameters are kept constant at standard parameters. CA measurements are performed 2 min and 6 min after the plasma treatment, respectively. The resulting CAs show increased surface energies, especially considering the polar part, which are independent of the plasma parameters ($U = 50 \ V - 300 \ V$, $P_W = 360 \ W - 625 \ W$) and the plasma treatment duration ($t = 5 \ s - 45 \ s$). The calculated total surface free energies as function of investigated

parameters are shown in Fig. 10. This suggests a fast change of the substrate surface energy and chemistry. The independence of the plasma treatment parameters on the detected surface energies could be due to the fast removal of top atomic layers by sputtering (approximately 0.3 nm/s). To detect a observable influence of the plasma treatment parameters, even shorter plasma treatment times might be necessary. Nevertheless, the rapid change in surface energy indicates great potential for applying the plasma treatment on steel strips in industrial applications, which require a combination of energy efficiency and fast surface treatments while limiting the heat input to the steel strip.

3.4. X-ray photoelectron spectroscopy (XPS)

XPS spectra of plasma treated surfaces are compared to reference surfaces, which are prepared identical as CA-reference samples. Plasma treatment is conducted at standard parameters except for the applied generator voltage U = 300 V and the plasma treatment time, which is doubled to t = 60 s. Prior to XPS analysis, all samples are exposed to air for approximately 20 min, allowing a native oxide layer to be reformed on the previously treated surfaces. Following initial XPS survey and high-resolution scans, samples are in-situ sputtered using a PHI Gas Cluster Ion Gun at 10 kV for t = 60 s. After in-situ sputtering, survey and high-resolution spectra are repeated. XPS survey scan spectra of plasma treated and reference surfaces are dominated by Fe, O, and C signals as indicated in Fig. 11. High resolution peaks further reveal presence of minor peaks assigned to Mn, Cr, Ca, Si, and N. XPS spectra of plasma treated and untreated sample surfaces are investigated via highresolution scans at the carbon (C 1s), oxygen (O 1s), and iron (Fe 2p) peak (Fig. 12). Trace elements contained in the investigated steel Mn, Si, Cr) show increased signals on plasma treated surfaces, while residue from preparative alkaline cleaning and transport atmosphere (Ca, S, N) are removed after the treatment.

Fig. 12(a) shows the individual peak fitting of C 1s, which consists of a dominant peak assigned to C-C/C-H (284.7 eV) and two less intense components originating from C—O (286.5 eV) and O-C=O (288.5 eV) bonds [51,52]. All components of the C 1s peak exhibit reduced peak areas on plasma treated surfaces, indicating a successful reduction of

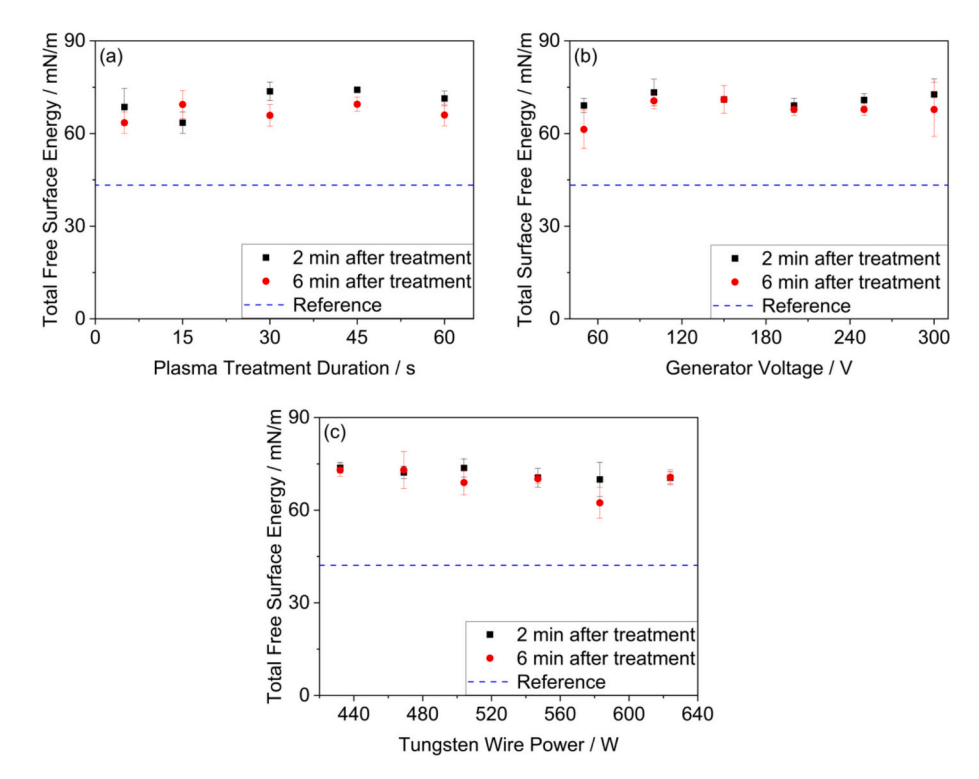


Fig. 10. Total free surface energy of plasma treated steel surface as function of (a) plasma treatment duration, (b) generator voltage and (c) tungsten wire power. Contact angle measurements are performed after 2 min and 6 min of atmospheric exposure time.

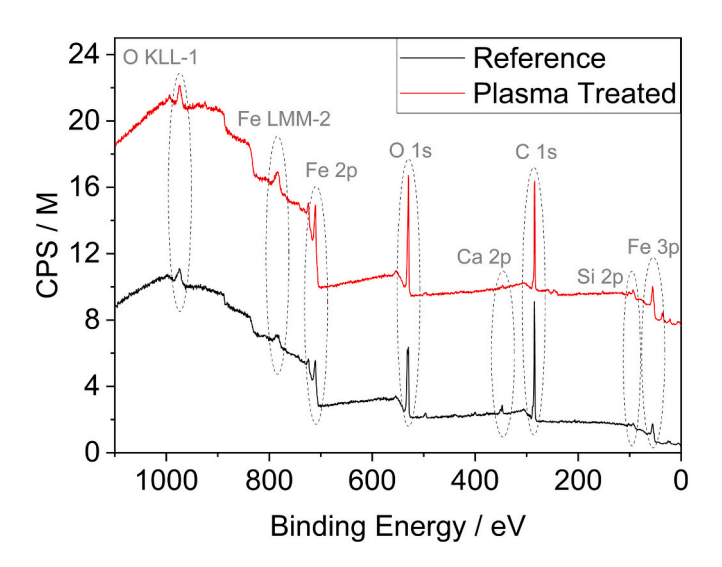


Fig. 11. XPS survey spectra of reference and plasma treated steel surface, which are dominated by Fe, C and O peaks. An offset has been applied to survey spectrum "plasma treated" for optical clarity.

carbonic components. The relative contribution of C-C/C-H bonds is increased indicating a lower recontamination during atmospheric exposure or higher sputter rates of C—O and O-C=O components, which probably origin from residue from alkaline cleaning performed prior to plasma treatments. After sputtering the surface in-situ via the sputter gun, C 1s signal is nearly eliminated, indicating a complete removal of carbon contamination of the surface. Individual peak fitting of oxygen spectra (Fig. 12(b)) reveals the contribution of lattice oxides $\rm O^{2-}$ being dominant at 530.1 eV, while two smaller shoulder peaks at 531.3 eV (OH_{at}) and 532.4 eV (OH_{ads}) originate from lattice and adsorbed hydroxides. Plasma treated surfaces show an increased amount of lattice oxides, while adsorbed hydroxides are reduced. This trend is enhanced

on plasma treated surfaces which are in-situ sputtered. The increase of O^{2-} is in good agreement with the increase of the Fe oxide signal observed in Fe 2p high resolution spectra, which indicates a reduction of C and O contamination layer on top of steel surfaces.

The Fe 2p spectra show a large and broad peak centered at approximately 710.5 eV and a smaller peak near 707 eV. The dominant component can be assigned to iron oxides and hydroxides present on the sample surface, including Fe₂O3, FeO, Fe₃O₄, and FeOOH, which all show overlapping peaks in XPS spectra difficult to distinguish [53–56]. The small peak is originating from metallic iron (Fe⁰) [16,53,57]. Due to the complexity of the iron oxide signal, a deconvolution of the peak is unreliable and not performed in this work. Instead, the iron oxide contribution is approximated with a single wide peak enabling a comparative assessment relative to the metallic Fe⁰ peak (706.7 eV). Plasma treatment increases the relative intensity of Fe⁰ signal compared to iron oxides, indicating a decrease in iron oxide thickness despite recontamination during air exposure prior to XPS analysis. A combination of plasma treatment and in-situ sputtering results in a further enhancement of Fe⁰ area up to 12 % relative contribution.

Utilizing a method proposed by Strohmeier [58] to estimate the thickness of continuous, thin oxide layers such as native oxides using the metallic and oxide component of the XPS signal [59–61]. The iron oxide thickness can be estimated via Eq. (3).

$$t = L\cos\theta \ln\left(1 + \frac{N_f I_0}{N_0 I_f}\right) \tag{3}$$

In this equation, t is the oxide layer thickness, θ is the electron emission angle, I_0 and I_f are the detected intensities of the film and substrate. L describes the effective attenuation length ($L_0=L_f=L=1.786$ nm, since photoelectrons from substrate and oxide possess similar energy), which is determined using NIST EAL database [62], and $N_f/N_0\approx 1.41$ [63] describes the ratio of volume atomic density of the film and the substrate. Using Eq. (3), the iron oxide layer thickness is determined from XPS measurements on reference samples, plasma treated and plasma treated & sputtered surfaces. The results are displayed in

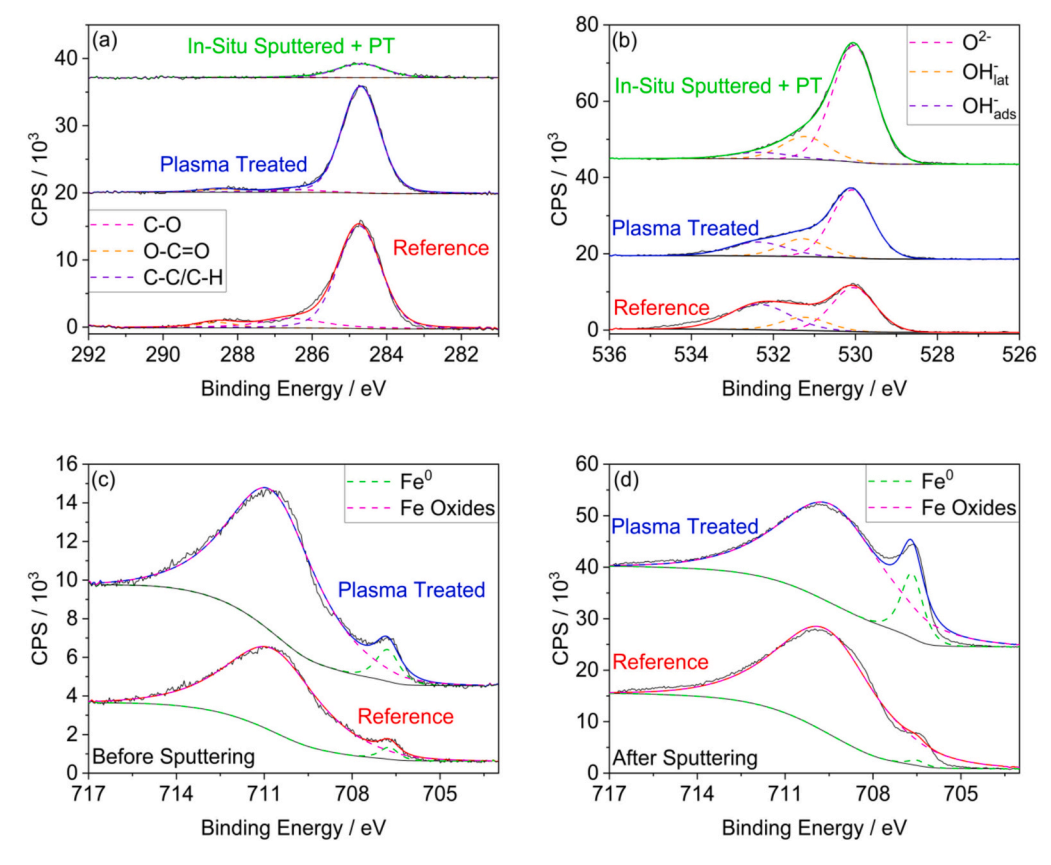


Fig. 12. (a) C 1s, (b) O 1s high resolution spectra of reference, plasma treated and plasma treated & in-situ sputtered surfaces with respective decompositions of the respective peaks. Fe 2p high resolution spectra are shown (c) before and (d) after in-situ sputtering. Baselines are offset due to clarification.

 $\begin{tabular}{ll} \textbf{Table 2} \\ Estimated iron oxide layer thickness using Eq. (3) on reference, plasma treated and plasma treated & sputtered surfaces. Uncertainties are estimated assuming 10 % error of effective attenuation length and XPS intensities. \\ \end{tabular}$

Sample	Oxide Layer Thickness (nm)
Reference	5.54 ± 0.80
Plasma Treated	4.00 ± 0.59
Plasma Treated & Sputtered	3.11 ± 0.47

Table 2. A reduction in iron oxide layer thickness is observed on plasma treated surfaces compared to untreated surfaces. This suggests that the reformation of the layer during atmospheric exposure results in a thinner oxide layer on plasma treated surfaces compared to reference surfaces. In-situ sputtering of plasma treated surfaces reduces the oxide layer thickness further, while the overall peak area of Fe⁰ and Fe oxides is strongly increased. This behavior is expected due to effective removal of top atomic layers consisting of hydrocarbons and -oxygens [64]. A shift of the oxide peak to shorter binding energies after sputtering indicates a change in iron oxide composition from Fe(III) to Fe (II) [54,64,65].

XPS analysis confirms the removal of carbon compounds from the sample surface and a reduction of oxide layer thickness by the plasma treatment. The oxide layer, which is reformed after plasma treatment during exposure to air, is estimated to be thinner compared to reference surfaces. An increase in iron oxide signal as well as O²⁻ signal indicates the effective removal of carbonic contamination via plasma treatment.

4. Summary

A simple and versatile plasma treatment chamber has been developed to prepare steel samples for subsequent manufacturing steps. The

chamber is characterized using optical emission spectroscopy which confirms sputtering of the sample surface. The electron temperature of the argon plasma is determined to be in the range of $T_e = 1$ eV to 2 eV, which is characteristic for technological plasmas in the converted pressure ($p \approx 10^{-3}$ mbar) and input power ranges ($P_A \approx 1 \text{ W cm}^{-2}$). Ion flux density and ion energy can be individually tuned by varying the generator voltage and the electron current emitted by the supportive electron emitter, a conductively heated tungsten wire, which ignites a supportive plasma discharge. The spatial distribution of the ion flux on the sample surface is determined utilizing a spatially resolved retarding field energy analyzer measurement. Results confirm expected patterns due to the anode tube geometry but shows small asymmetries likely caused by magnetic field variations. Plasma treated steel surfaces are characterized via contact angle measurements, revealing a strong increase in surface free energy after just t = 5 s of plasma treatment applying an ion flux density $J_i \approx 4.5 \text{ A m}^{-2}$ with ion energies $E \approx 420 \text{ eV}$. This rapid improvement highlights its suitability for industrial applications, particularly in enhancing wettability to prepare surfaces for coating processes. XPS analysis confirms the reduction of carbon compounds as well as Fe oxide layer thickness by the plasma treatment even after exposure to atmospheric conditions. This indicates durable improvements that maintain their benefits over time, making the treatment highly effective for industrial use.

In summary, this plasma treatment system offers a versatile and efficient approach to enhancing steel surface properties, with significant potential for streamlining processes in manufacturing environments where rapid and consistent surface preparation is critical, even though the challenges of inhomogeneity of the plasma treatment must be overcome for implementing the technique in an industrial production line. One possible step for successful upscaling could be to place several electron emitter wires in the system, or replace the supportive discharge with an ICP plasma, which could be combined with a pulsed-DC bias to

tune the ion energy bombardment of the steel surface.

CRediT authorship contribution statement

Gustav Gürtler: Writing – original draft, Visualization, Methodology, Investigation, Formal analysis, Data curation, Conceptualization. Wolfgang Burgstaller: Writing – review & editing, Supervision, Project administration. Friedrich Aumayr: Writing – review & editing, Supervision. Markus Valtiner: Writing – review & editing, Supervision, Conceptualization.

Funding sources

This research did not receive any specific grant from funding agencies in the public, commercial, or not-for-profit sectors.

Declaration of competing interest

The authors declare that they have no known competing financial interests or personal relationships that could have appeared to influence the work reported in this paper.

Acknowledgments

The authors are grateful to Tatjana Ott for assistance with the XPS measurements.

Data availability

The data that has been used is confidential.

References

- [1] X. Lu, P.J. Bruggeman, S. Reuter, G. Naidis, A. Bogaerts, M. Laroussi, M. Keidar, E. Robert, J.-M. Pouvesle, D. Liu, K. (Ken) Ostrikov, Grand challenges in low temperature plasmas, Front. Phys. 10 (2022), https://doi.org/10.3389/ fphy.2022.1040658.
- [2] R. Walden, A. Goswami, L. Scally, G. McGranaghan, P.J. Cullen, S.C. Pillai, Nonthermal plasma technologies for advanced functional material processing and current applications: opportunities and challenges, J. Environ. Chem. Eng. 12 (2024) 113541, https://doi.org/10.1016/j.jece.2024.113541.
- [3] L. Bárdos, H. Baránková, Plasma processes at atmospheric and low pressures, Vacuum 83 (2008) 522–527, https://doi.org/10.1016/j.vacuum.2008.04.063.
- [4] D.S. Patil, R. Kar, S.S. Chopade, Chapter 12 cold plasma processing of materials for extreme conditions, in: A.K. Tyagi, S. Banerjee (Eds.), Materials under Extreme Conditions, Elsevier, Amsterdam, 2017, pp. 411–469, https://doi.org/10.1016/ B978-0-12-801300-7.00012-7.
- [5] C. Ruzafa-Silvestre, P. Carbonell-Blasco, E. Orgiles-Calpena, F. Aran Ais, Low-pressure plasma treatment applied to polymeric materials for a sustainable footwear industry, in: Proceedings of the 8th International Conference on Advanced Materials and Systems, INCDTP Leather and Footwear Research Institute (ICPI), Bucharest, Romania, 2020, pp. 455–460, https://doi.org/10.24264/icams-2020.IV.19.
- [6] C. Mandolfino, E. Lertora, C. Gambaro, M. Pizzorni, Functionalization of neutral polypropylene by using low pressure plasma treatment: effects on surface characteristics and adhesion properties, Polymers 11 (2019) 202, https://doi.org/ 10.3390/polym11020202.
- [7] M.R.S. McCoustra, R.R. Mather, Plasma modification of textiles: understanding the mechanisms involved, Text. Prog. 50 (2018) 185–229, https://doi.org/10.1080/ 00405167.2019.1637115.
- [8] M.A. Mackinder, K. Wang, B. Zheng, M. Shrestha, Q.H. Fan, Magnetic field enhanced cold plasma sterilization, Clin. Plasma Med. 17–18 (2020) 100092, https://doi.org/10.1016/j.cpme.2019.100092.
- [9] H. Halfmann, N. Bibinov, J. Wunderlich, P. Awakowicz, A double inductively coupled plasma for sterilization of medical devices, J. Phys. D. Appl. Phys. 40 (2007) 4145. https://doi.org/10.1088/0022-3727/40/14/008.
- [10] E. Muratov, F.P. Rosenbaum, F.M. Fuchs, N.J. Ulrich, P. Awakowicz, P. Setlow, R. Moeller, Multifactorial resistance of Bacillus subtilis spores to low-pressure plasma sterilization, Appl. Environ. Microbiol. 90 (2024), https://doi.org/ 10.1128/aem.01329-23.
- [11] H. Jansen, H. Gardeniers, M. de Boer, M. Elwenspoek, J. Fluitman, A survey on the reactive ion etching of silicon in microtechnology, J. Micromech. Microeng. 6 (1996) 14, https://doi.org/10.1088/0960-1317/6/1/002.
- [12] H. Abe, M. Yoneda, N. Fujiwara, Developments of plasma etching technology for fabricating semiconductor devices, Jpn. J. Appl. Phys. 47 (2008) 1435, https://doi. org/10.1143/JJAP.47.1435.

- D.J. Economou, Pulsed plasma etching for semiconductor manufacturing, J. Phys.
 D. Appl. Phys. 47 (2014), https://doi.org/10.1088/0022-3727/47/30/303001.
- [14] H. Aghajani, S. Behrangi, Introduction, in: H. Aghajani, S. Behrangi (Eds.), Plasma Nitriding of Steels, Springer International Publishing, Cham, 2017, pp. 1–8, https://doi.org/10.1007/978-3-319-43068-3_1.
- [15] C.J. Scheuer, R.P. Cardoso, S.F. Brunatto, An overview on plasma-assisted thermochemical treatments of martensitic stainless steels*, Surf. Topogr. Metrol. Prop. 11 (2023) 013001, https://doi.org/10.1088/2051-672X/acb372.
- [16] N. Kalel, A. Darpe, J. Bijwe, Low pressure plasma induced surface changes of some stainless steels, Surf. Coat. Technol. 425 (2021) 127700, https://doi.org/10.1016/ j.surfcoat.2021.127700.
- [17] K. Terpilowski, D. Rymuszka, L. Holysz, M. Ilnicki, Surface properties of metal alloys used in aviation after plasma treatment, Surf. Interface Anal. 49 (2017) 647–653, https://doi.org/10.1002/sia.6204.
- [18] S.A. Fadeev, A.I. Saifutdinov, N.F. Kashapov, Efficiency of surface cleaning by a glow discharge for plasma spray coating, J. Phys. Conf. Ser. 669 (2016) 012010, https://doi.org/10.1088/1757-899X/134/1/012010.
- [19] D.F. O'Kane, K.L. Mittal, Plasma cleaning of metal surfaces, J. Vac. Sci. Technol. 11 (1974) 567–569, https://doi.org/10.1116/1.1318069.
- [20] A. Belkind, S. Krommenhoek, H. Li, Z. Orban, F. Jansen, Removal of oil from metals by plasma techniques, Surf. Coat. Technol. 68–69 (1994) 804–808, https://doi. org/10.1016/0257-8972(94)90257-7.
- [21] Y.-S. Lin, C.-H. Chang, T.-J. Huang, Enhanced corrosion protection of cold rolled steel by low-temperature plasma cleaning and plasma polymerization, Surf. Coat. Technol. 200 (2006) 4929–4938, https://doi.org/10.1016/j.surfcoat.2005.05.015.
- [22] Y. Deng, W. Chen, B. Li, C. Wang, T. Kuang, Y. Li, Physical vapor deposition technology for coated cutting tools: a review, Ceram. Int. 46 (2020) 18373–18390, https://doi.org/10.1016/j.ceramint.2020.04.168.
- [23] A. Dan, P.K. Bijalwan, A.S. Pathak, A.N. Bhagat, A review on physical vapor deposition-based metallic coatings on steel as an alternative to conventional galvanized coatings, J. Coat. Technol. Res. 19 (2022) 403–438, https://doi.org/ 10.1007/s11998-021-00564-z.
- [24] D. Landek, S. Jakovljević, V. Alar, S. Kovačić, Effect of steel substrate on the corrosion properties of a gradient multilayer TiN/TiCN coating deposited by the PACVD process, Mater. Corros. 70 (2019) 307–318, https://doi.org/10.1002/ maco.201810358.
- [25] E. Vassallo, A. Cremona, L. Laguardia, E. Mesto, Preparation of plasma-polymerized SiOx-like thin films from a mixture of hexamethyldisiloxane and oxygen to improve the corrosion behaviour, Surf. Coat. Technol. 200 (2006) 3035–3040, https://doi.org/10.1016/j.surfcoat.2004.11.001.
- [26] N. Giannakaris, G. Gürtler, T. Stehrer, M. Mair, J.D. Pedarnig, Optical emission spectroscopy of an industrial thermal atmospheric pressure plasma jet: parametric study of electron temperature, Spectrochim. Acta B At. Spectrosc. 207 (2023) 106736, https://doi.org/10.1016/j.sab.2023.106736.
- [27] F. Schlichting, H. Kersten, A retarding field thermal probe for combined plasma diagnostics, EPJ Tech. Instrum. 10 (2023) 19, https://doi.org/10.1140/epjti/ s40485-023-00106-4.
- [28] D. Gahan, S. Daniels, C. Hayden, P. Scullin, D. O'Sullivan, Y.T. Pei, M.B. Hopkins, Ion energy distribution measurements in rf and pulsed dc plasma discharges, Plasma Sources Sci. Technol. 21 (2012) 024004, https://doi.org/10.1088/0963-0252/21/2/024004.
- [29] S.A. Voronin, M.R. Alexander, J.W. Bradley, Time-resolved measurements of the ion energy distribution function in a pulsed discharge using a double gating technique, Meas. Sci. Technol. 16 (2005) 2446, https://doi.org/10.1088/0957-0233/16/12/007.
- [30] D. Gahan, B. Dolinaj, M.B. Hopkins, Comparison of plasma parameters determined with a Langmuir probe and with a retarding field energy analyzer, Plasma Sources Sci. Technol. 17 (2008) 035026, https://doi.org/10.1088/0963-0252/17/3/ 035026.
- [31] T. Baloniak, R. Reuter, C. Flötgen, A. Von Keudell, Calibration of a miniaturized retarding field analyzer for low-temperature plasmas: geometrical transparency and collisional effects, J. Phys. D. Appl. Phys. 43 (2010) 055203, https://doi.org/ 10.1088/0022-3727/43/5/055203.
- [32] NIST Atomic Spectra Database, NIST Atomic Spectra Database. https://www.nist.gov/pml/atomic-spectra-database, 2009 (accessed February 10, 2025).
- [33] Atomic spectral line database from CD-ROM 23 of R. L. Kurucz., (n.d.). https://lweb.cfa.harvard.edu/amp/ampdata/kurucz23/sekur.html (accessed March 25, 2025).
- [34] C. Corbella, M. Rubio-Roy, E. Bertran, S. Portal, E. Pascual, M.C. Polo, J.L. Andújar, Ion energy distributions in bipolar pulsed-dc discharges of methane measured at the biased cathode, Plasma Sources Sci. Technol. 20 (2011) 015006, https://doi. org/10.1088/0963-0252/20/1/015006.
- [35] M. Jin, R. Sanedrin, D. Frese, C. Scheithauer, T. Willers, Replacing the solid needle by a liquid one when measuring static and advancing contact angles, Colloid Polym. Sci. 294 (2016) 657–665, https://doi.org/10.1007/s00396-015-3823-1.
- [36] G. As, S. Georgiev, P. Baluschev, M. Eftimov, K. Landfester Bacheva, Addressing the apparent controversies between the contact angle-based models for estimation of surface free energy: a critical review, Coll. Interfac. 8 (2024) 62, https://doi.org/ 10.3390/colloids8060062.
- [37] V.M. Donnelly, Plasma electron temperatures and electron energy distributions measured by trace rare gases optical emission spectroscopy, J. Phys. D. Appl. Phys. 37 (2004) R217–R236, https://doi.org/10.1088/0022-3727/37/19/R01.
- [38] F.J. Gordillo-Vázquez, M. Camero, C. Gómez-Aleixandre, Spectroscopic measurements of the electron temperature in low pressure radiofrequency Ar/H $_2$ /Cl $_4$ plasmas used for the synthesis of nanocarbon structures,

- Plasma Sources Sci. Technol. 15 (2006) 42–51, https://doi.org/10.1088/0963-0252/15/1/007
- [39] F.U. Khan, N.U. Rehman, S. Naseer, M.A. Naveed, A. Qayyum, N.A.D. Khattak, M. Zakaullah, Diagnostic of 13.56 MHz RF sustained Ar–N 2 plasma by optical emission spectroscopy, Eur. Phys. J. Appl. Phys. 45 (2009) 11002, https://doi.org/ 10.1051/epiar/2008198
- [40] H. Akatsuka, Optical Emission Spectroscopic (OES) analysis for diagnostics of electron density and temperature in non-equilibrium argon plasma based on collisional-radiative model, Adv. Phys. X 4 (2019) 1592707, https://doi.org/ 10.1080/23746149.2019.1592707.
- [41] N. Tian-Ye, C. Jin-Xiang, L. Lei, L. Jin-Ying, W. Yan, W. Liang, L. You, A comparison among optical emission spectroscopic methods of determining electron temperature in low pressure argon plasmas, Chin. Phys. 16 (2007) 2757–2763, https://doi.org/10.1088/1009-1963/16/9/043.
- [42] J.B. Boffard, B. Chiaro, T. Weber, C.C. Lin, Electron-impact excitation of argon: optical emission cross sections in the range of 300–2500nm, At. Data Nucl. Data Tables 93 (2007) 831–863, https://doi.org/10.1016/j.adt.2007.06.004.
- [43] H. Park, W. Choe, Parametric study on excitation temperature and electron temperature in low pressure plasmas, Curr. Appl. Phys. 10 (2010) 1456–1460, https://doi.org/10.1016/j.cap.2010.05.013.
- [44] H. Mishra, M. Tichý, P. Kudrna, Optical emission spectroscopy study of plasma parameters in low-pressure hollow cathode plasma jet and planar magnetron powered by DC and pulsed DC supply, Vacuum 205 (2022) 111413, https://doi. org/10.1016/j.vacuum.2022.111413.
- [45] R.L. Rhoades, S.M. Gorbatkin, Characterization of Ar/Cu electron-cyclotron-resonance plasmas using optical emission spectroscopy, J. Appl. Phys. 80 (1996) 2605–2613. https://doi.org/10.1063/1.363177.
- [46] N. Derkaoui, C. Rond, T. Gries, G. Henrion, A. Gicquel, Determining electron temperature and electron density in moderate pressure H₂/CH₄ microwave plasma, J. Phys. D. Appl. Phys. 47 (2014) 205201, https://doi.org/10.1088/0022-3727/47/20/205201
- [47] K. Kano, M. Suzuki, H. Akatsuka, Spectroscopic measurement of electron temperature and density in argon plasmas based on collisional-radiative model, Plasma Sources Sci. Technol. 9 (2000) 314–322, https://doi.org/10.1088/0963-0252/9/3/309.
- [48] D. Gahan, B. Dolinaj, C. Hayden, M.B. Hopkins, Retarding field analyzer for ion energy distribution measurement through a radio-frequency or pulsed biased sheath, Plasma Process. Polym. 6 (2009) S643–S648, https://doi.org/10.1002/ ppap. 200931607
- [49] Y.-R. Zhang, Z.-Z. Zhao, C. Xue, F. Gao, Y.-N. Wang, Ion energy and angular distributions in planar Ar/O2 inductively coupled plasmas: hybrid simulation and experimental validation, J. Phys. D. Appl. Phys. 52 (2019) 295204, https://doi. org/10.1088/1361-6463/ab1dd3.
- [50] C. Hayden, D. Gahan, M.B. Hopkins, Ion energy distributions at a capacitively and directly coupled electrode immersed in a plasma generated by a remote source, Plasma Sources Sci. Technol. 18 (2009) 025018, https://doi.org/10.1088/0963-0252/18/2/025018.

- [51] S. Feliu Jr., M.L. Pérez-Revenga, Effect of alloying elements (Ti, Nb, Mn and P) and the water vapour content in the annealing atmosphere on the surface composition of interstitial-free steels at the galvanising temperature, Appl. Surf. Sci. 229 (2004) 112–123, https://doi.org/10.1016/j.apsusc.2004.01.047.
- [52] G. Kurbatov, E. Darque-Ceretti, M. Aucouturier, Characterization of hydroxylated oxide film on iron surfaces and its acid-base properties using XPS, Surf. Interface Anal. 18 (1992) 811–820, https://doi.org/10.1002/sia.740181206.
- [53] M.C. Biesinger, B.P. Payne, A.P. Grosvenor, L.W.M. Lau, A.R. Gerson, R.S.T. C. Smart, Resolving surface chemical states in XPS analysis of first row transition metals, oxides and hydroxides: Cr, Mn, Fe, Co and Ni, Appl. Surf. Sci. 257 (2011) 2717–2730, https://doi.org/10.1016/j.apsusc.2010.10.051.
- [54] W. Xu, K. Daub, X. Zhang, J.J. Noel, D.W. Shoesmith, J.C. Wren, Oxide formation and conversion on carbon steel in mildly basic solutions, Electrochim. Acta 54 (2009) 5727–5738, https://doi.org/10.1016/j.electacta.2009.05.020.
- [55] A.P. Grosvenor, B.A. Kobe, M.C. Biesinger, N.S. McIntyre, Investigation of multiplet splitting of Fe 2p XPS spectra and bonding in iron compounds, Surf. Interface Anal. 36 (2004) 1564–1574, https://doi.org/10.1002/sia.1984.
- [56] N. Fairley, P. Bargiela, W.-M. Huang, J. Baltrusaitis, Principal Component Analysis (PCA) unrawels spectral components present in XPS spectra of complex oxide films on iron foil, Appl. Surf. Sci. Adv. 17 (2023) 100447, https://doi.org/10.1016/j. apsadv.2023.100447.
- [57] C.S. Doyle, C.K. Seal, B.J. James, Evolution of steel surface composition with heating in vacuum and in air, Appl. Surf. Sci. 257 (2011) 10005–10017, https://doi.org/10.1016/j.apsusc.2011.06.128.
- [58] B.R. Strohmeier, An ESCA method for determining the oxide thickness on aluminum alloys, Surf. Interface Anal. 15 (1990) 51–56, https://doi.org/10.1002/ sia 740150109
- [59] G. Greczynski, L. Hultman, A step-by-step guide to perform X-ray photoelectron spectroscopy, J. Appl. Phys. 132 (2022) 011101, https://doi.org/10.1063/ 5.0086359.
- [60] S. Detriche, S. Vivegnis, J.-F. Vanhumbeeck, A. Felten, P. Louette, F.U. Renner, J. Delhalle, Z. Mekhalif, XPS fast depth profile of the native oxide layers on AISI 304, 316 and 430 commercial stainless steels and their evolution with time, J. Electron Spectrosc. Relat. Phenom. 243 (2020) 146970, https://doi.org/ 10.1016/j.elspec.2020.146970.
- [61] C.J. Powell, Practical guide for inelastic mean free paths, effective attenuation lengths, mean escape depths, and information depths in X-ray photoelectron spectroscopy, J. Vac. Sci. Technol. A 38 (2020) 023209, https://doi.org/10.1116/ 1.5141079.
- [62] Powell, C.J., A. Jablonski, NIST Standard Reference Database 82, Version 1.3 (n.d.). doi:10.18434/T4MK5P.
- [63] Weast Robert C., CRC Handbook of Chemistry and Physics, CRC Press, n.d.
- [64] M. Flori, B. Gruzza, L. Bideux, G. Monier, C. Robert-Goumet, A study of the 42CrMo4 steel surface by quantitative XPS electron spectroscopy, Appl. Surf. Sci. 254 (2008) 4738–4743. https://doi.org/10.1016/j.apsusc.2008.01.090.
- [65] T. Yamashita, P. Hayes, Analysis of XPS spectra of Fe2+ and Fe3+ ions in oxide materials, Appl. Surf. Sci. 254 (2008) 2441–2449, https://doi.org/10.1016/j. apsusc.2007.09.063.